




## Open Archive TOULOUSE Archive Ouverte (OATAO)

OATAO is an open access repository that collects the work of Toulouse researchers and makes it freely available over the web where possible.

This is an author-deposited version published in : <http://oatao.univ-toulouse.fr/>  
Eprints ID : 19956

**To link to this article:** DOI: 10.1016/j.applthermaleng.2017.02.050  
URL : <http://dx.doi.org/10.1016/j.applthermaleng.2017.02.050>

**To cite this version** : Nishikawara, Masahito and Nagano, Hosei and Prat, Marc  *Numerama study on heat-transfer characteristics of loop heat pipe evaporator using three-dimensional pore network model.* (2017) Applied Thermal Engineering, vol. 126. pp. 1098-1106. ISSN 1359-4311

Any correspondence concerning this service should be sent to the repository administrator: [staff-oatao@listes-diff.inp-toulouse.fr](mailto:staff-oatao@listes-diff.inp-toulouse.fr)

Research Paper

# Numerical study on heat-transfer characteristics of loop heat pipe evaporator using three-dimensional pore network model

Masahito Nishikawara <sup>a,\*</sup>, Hosei Nagano <sup>b</sup>, Marc Prat <sup>c</sup>

<sup>a</sup> Department of Mechanical Engineering, Toyohashi University of Technology, 1-1 Hibarigaoka, Tenpaku-cho, Toyohashi, Aichi 441-8580, Japan

<sup>b</sup> Department of Aerospace Engineering, Nagoya University, Japan

<sup>c</sup> Université de Toulouse, INPT, UPS, IMFT, Toulouse, France

## A B S T R A C T

An important consideration while designing the shape of a capillary evaporator is the phase distribution in the wick. However, the distribution depends on the working fluids and porous materials. This study investigates the heat-transfer characteristics of a loop heat pipe (LHP) evaporator by using a three-dimensional pore network model with a dispersed pore size wick. The simulation considers saturated and unsaturated wicks. A stainless steel (SS)-ammonia, polytetrafluoroethylene (PTFE)-ammonia, and copper-water LHP are simulated. The copper-water LHP has the highest transition heat flux to the unsaturated wick. When the optimum evaporator shape of the copper-water LHP is designed, it is reasonable to assume that the phase state is saturated. On the other hand, for the ammonia LHP design, the state is assumed to be unsaturated. Simulation results show the heat-transfer structure in the evaporator and indicate that the applied heat flux concentrates on the three-phase contact line (TPCL) within the case, wick, and grooves. An evaporator configuration with circumferential and axial grooves is simulated to investigate the effect of the TPCL length. Results indicate that the optimum shape can be realized by varying the TPCL length. The proposed method is expected to serve as a simple approach to design an evaporator.

## 1. Introduction

Loop heat pipes (LHPs) and capillary pumped loops are widely used to achieve thermal control in various applications such as spacecraft, automobiles, computers, LED-based devices, and power semiconductor devices. The thermal resistance of an LHP is the sum of the thermal resistances of the evaporator and condenser. The evaporator thermal resistance is based on two-phase flow in a porous structure with a phase change. There have been many reports on two-dimensional evaporator simulations [1–4], and recently, a more accurate three-dimensional model was developed [5–12]. Depending on the heat flux applied to the evaporator, the wick phase state is divided into a saturated state with a liquid phase and an unsaturated state with liquid and vapor phases, as shown in Fig. 1. Chernysheva and Maydanik [5,6] determined the shape of the liquid–vapor interface based on the local temperature of the wick but ignored the evaporation at the liquid–vapor

interface in the wick. On the other hand, other studies [1–4,8,9] were based on the maximum capillary pressure and considered the evaporation within the wick. In a copper-water LHP [5,6], an unsaturated state was not formed at less than 100 W/cm<sup>2</sup>. However, in an ammonia LHP [8], an unsaturated state was formed at more than 1 W/cm<sup>2</sup>. The threshold of the transition heat flux is different because it depends on the working fluid and wick thermal conductivity. Table 1 lists the transition heat flux for an unsaturated wick in different studies. Among the cited studies, only Refs. [2,13] present experimental results; the others present results based on numerical simulations. In the simulations, the condition for transition to an unsaturated state is given by

$$T - T_{sat} \equiv \Delta T_{sup} > \Delta T_{nuc} \quad (1)$$

where  $T$  is the wick temperature,  $T_{sat}$  is the saturation temperature,  $\Delta T_{sup}$  is the superheat of the wick, and  $\Delta T_{nuc}$  is the threshold of nucleation. The nucleation superheat is considered to be a constant in some studies, whereas it is calculated in others. For example, in Refs. [3,8], the nucleation superheat is considered as 4 °C. However, because nucleation superheat depends on the working fluid and

\* Corresponding author.

E-mail address: [nishikawara@me.tut.ac.jp](mailto:nishikawara@me.tut.ac.jp) (M. Nishikawara).

## Nomenclature

$A$	area (m <sup>2</sup> )	$P$	pressure (Pa)
$\Delta P_{int}$	pressure difference at liquid–vapor interface (Pa)	$P_{cap\_max}$	maximum capillary pressure (Pa)
$\Delta T_{sup}$	superheat of liquid phase (K)	$P_{gr}$	groove pressure (Pa)
$\Delta T_{nuc}$	boiling incipient superheat (K)	$\dot{q}_{apply}$	applied heat flux (W/m <sup>2</sup> )
$h_c$	convective heat-transfer coefficient (W/m <sup>2</sup> ·K)	$r$	bubble radius (m)
$h_{evap}$	evaporator heat-transfer coefficient (W/m <sup>2</sup> ·K)	$r_{th}$	throat radius (m)
$h_i$	interfacial heat-transfer coefficient (W/m <sup>2</sup> ·K)	$T$	temperature (K)
$H_{fg}$	latent heat (J/kg)	$T_{e\_max}$	the maximum temperature the case (K)
$k_{eff}$	effective thermal conductivity (W/m·K)	$T_{gr}$	groove temperature (K)
$k_{eff,l}$	effective thermal conductivity of liquid phase (W/m·K)	$T_{sat}$	saturation temperature (K)
$k_{eff,v}$	effective thermal conductivity of vapor phase (W/m·K)	$\sigma$	surface tension (N/m)
$\dot{m}_n$	mass flow rate for normal direction (kg/s)	$\rho_{-v}$	vapor density (kg/m <sup>3</sup> )
$n$	normal direction (m)	$\theta$	contact angle (rad)

nucleus state, its estimation is difficult. Therefore, to obtain an optimum design for the evaporator shape, the thermal characteristics of the saturated state are important in some cases whereas those of the unsaturated state are important in others, depending on the working fluid and the configuration of the evaporator. In this study, a numerical model of an LHP evaporator was developed using

a pore network model; then, the transition heat flux in some evaporator configurations and the heat-transfer structure in both states of the wick were investigated.

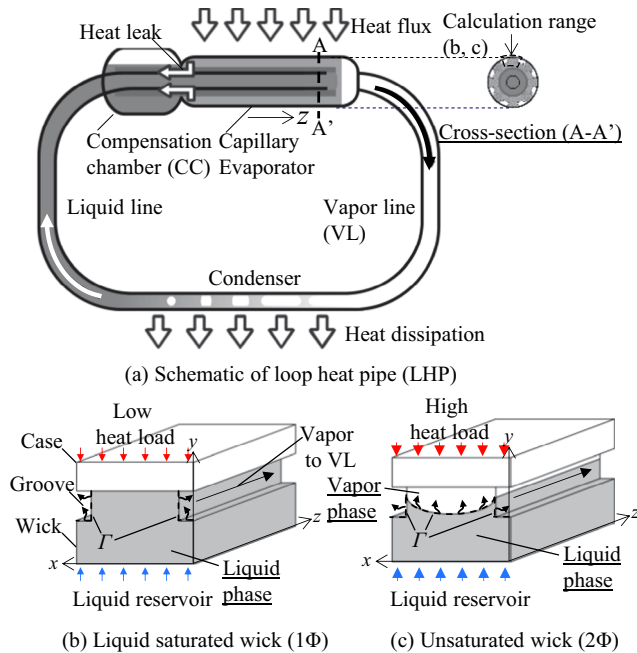


**Fig. 1.** Behavior of phase distribution in LHP wick.  $\Gamma$  is evaporation interface. Capillary pressure is developed at  $\Gamma$ .

**Table 1**

Transition heat flux for unsaturated wick in different studies. Exp. indicates experimental results.

Study	Working fluid	Wick bulk thermal conductivity, W/m·K	Pore radius, $\mu\text{m}$	Transition heat flux, W/cm <sup>2</sup>
Figus et al. [1]	Ammonia	0.4, 10, 0.5	10	<0.45
Kaya and Goldak [3]	Ammonia	14.5	1.2	0.1254–0.3762
Wan et al. [4]	Ammonia	15.2, 90.4	–	<4
Mottet et al. [8]	Ammonia	4.18	1	1
Zhao and Liao [2] (Exp.)	Water	0.78	256	17.72
Chernysheva and Maydanik [6]	Water	That of copper	21	100–111
Hatakenaka et al. [13] (Exp.)	Water	That of stainless steel	2.8	<1.69
Mottet et al. [8]	FC3284	46	550	0.5
Nishikawara et al. [9]	Ethanol	0.25	1.2	1.25

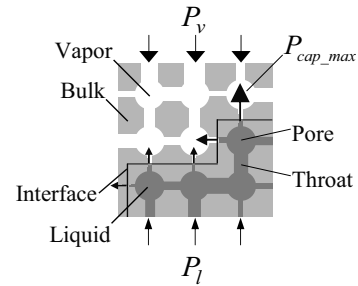


**Fig. 2.** Sketch of pore network and liquid-vapor interface balance.

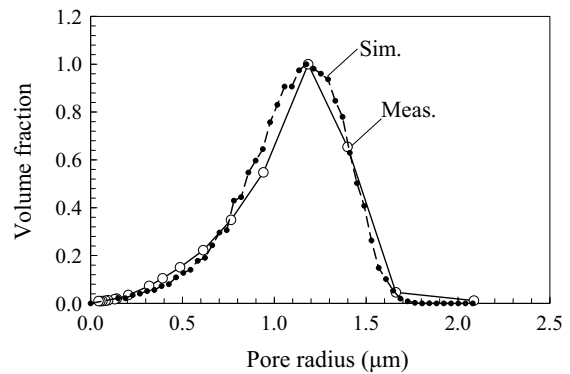


**Fig. 3.** Pore radius distribution used in the simulation. Simulation value is used in throat radius  $r_{th}$ . Measurement value is obtained by mercury intrusion method.

2. Numerical model

Here, a three-dimensional mathematical model using a pore network is presented. Sketch of the lattice pore network is shown in Fig. 2. The network consists of pores and throats. This pore network model can consider the pore radius distribution in the wick. The radius distribution used in the model is shown in Fig. 3 and is generated based on measurement results obtained by the mercury intrusion method. The model details are described in Refs. [9–12]. Fig. 4 shows the flowchart for the numerical solution process. First, the thermal-hydraulics states of a liquid saturated wick (1Φ) are solved. Here, system of equations of pressure based on pore network and energy conservation including convection term are solved. Then, temperature, pressure and liquid velocity are obtained. If the superheat of the liquid phase at the contact surface between the wick and case exceeds the nucleation superheat, the

phase state becomes unsaturated. Transition from a saturated state to an unsaturated state is determined as follows:

$$\Delta T_{sup} > \Delta T_{nuc} = \frac{2\sigma T_{sat}}{\rho_v r H_{fg}} \quad (2)$$

where  $\Delta T_{sup}$  is the superheat of the liquid phase in the wick,  $\Delta T_{nuc}$  is the boiling incipient superheat,  $\sigma$  is the surface tension,  $T_{sat}$  is the saturation temperature,  $\rho_v$  is the density of the vapor,  $r$  is the radius of the bubbles, and  $H_{fg}$  is the latent heat. In this model,  $r$  is the mode pore radius of the wick and is 1.2 μm from Fig. 3. After vapor nucleation occurs, a vapor phase forms at the contact surface

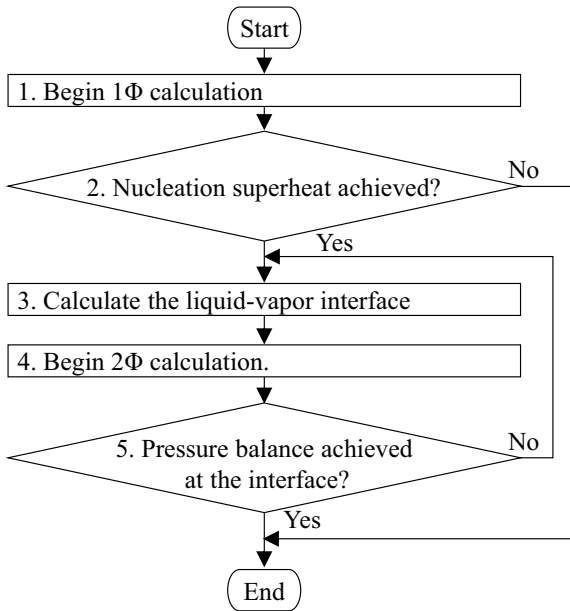


Fig. 4. Flowchart of numerical solution process.

Table 2 Configuration of evaporator used in simulations.

Simulation no.	Wick material	Working fluid	Wick shape
1	Stainless steel	Ammonia	Only axial grooves
2	PTFE	Ammonia	Only axial grooves
3	Copper	Water	Only axial grooves
4	Stainless steel	Ammonia	Axial + circumferential grooves
5	PTFE	Ammonia	Axial + circumferential grooves
6	Copper	Water	Axial + circumferential grooves

Table 3 Transition heat flux for unsaturated wick in different evaporator configurations.

Evaporator configuration	Transition heat flux, W/cm <sup>2</sup>
Stainless steel-ammonia	1.25
PTFE-ammonia	<0.3125
Copper-water	4.375

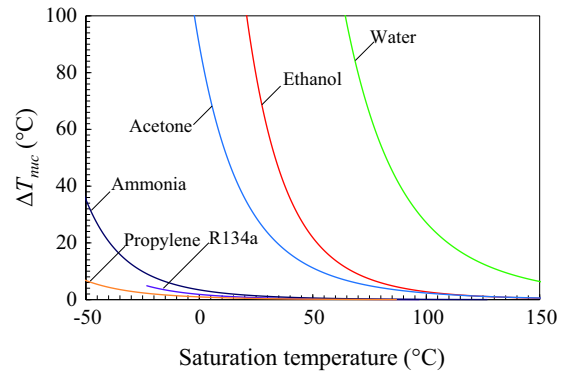


Fig. 5. Boiling incipient superheat for each working fluid (r = 1.2 μm).

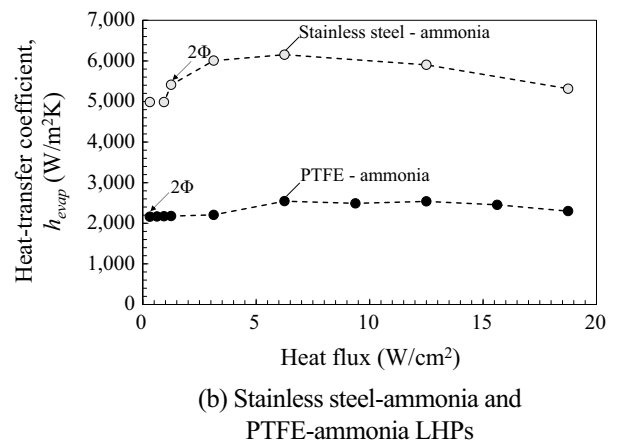
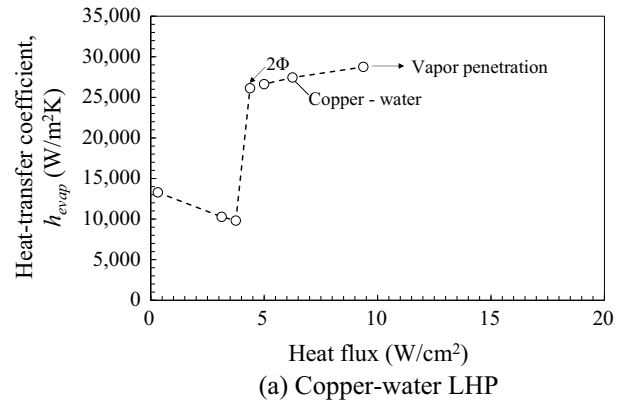


Fig. 6. Evaporator heat-transfer coefficient as function of heat flux.

between the wick and case until the vapor contacts the grooves. Next, the thermal-hydraulics states of an unsaturated wick ( $2\Phi$ ) are solved. When the pressure difference between the vapor and liquid phases at the interface in the wick,  $\Delta P_{int}$ , exceeds the maximum capillary pressure in the pore throat, the vapor phase displaces the liquid phase, as expressed in Eq. (3):

$$\Delta P_{int} > P_{cap\_max} = \frac{2\sigma \cos \theta}{r_{th}} \quad (3)$$

where  $P_{cap\_max}$  is the maximum capillary pressure,  $\theta$  is the contact angle, and  $r_{th}$  is cylinder radius of the throat as shown in Fig. 2. The calculation is iterated until all the interfaces satisfy Eq. (3). In the saturated wick, liquid evaporates on the groove-wick interface, and in the saturated wick, liquid evaporates within the wick and on the groove-wick liquid-vapor interface.

### 3. Results and discussion for classical evaporator shape

The numerical model was validated by comparing its results with the experimental results obtained using a polytetrafluo-

roethylene (PTFE)-ethanol LHP [9]. Wettability of PTFE is generally hydrophobic, however in some fluid combinations with ammonia, ethanol, etc., the wettability is hydrophilic. The contact angle

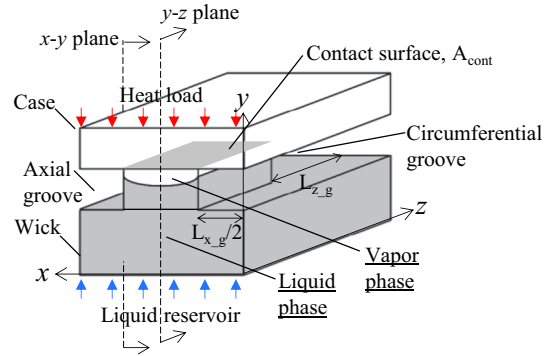


Fig. 8. Schematic of computational domain of three-dimensional groove shape.

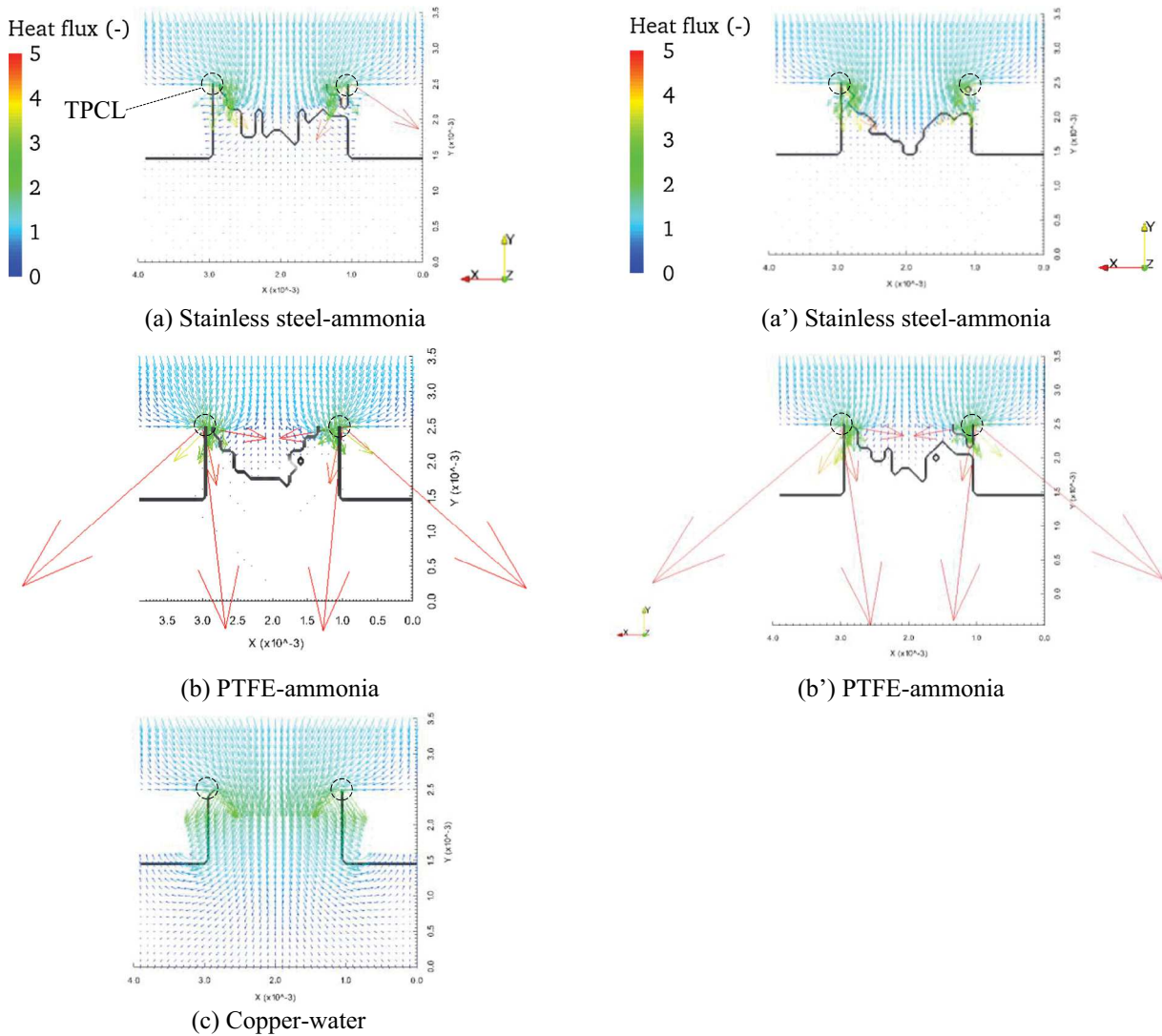


Fig. 7. Distribution of heat flux vectors and liquid-vapor interface shape on the x-y plane. The color bar is normalized with an applied heat flux. The applied heat fluxes are  $6.25 \text{ W/cm}^2$  in (a, b, c) and  $12.5 \text{ W/cm}^2$  in (a', b'). Only axial grooves are created. The TPCL length is  $500 \text{ m}^{-1}$ . No data in (c') due to vapor penetration. (For interpretation of the references to color in this figure legend, the reader is referred to the web version of this article.)

between PTFE and ethanol was  $30^\circ$ , which was measured by using a contact angle meter (KYOWA DM-301). The dimensions of the evaporator mentioned in this section are similar to the dimensions considered in the validation. The simulation is performed by changing the bulk thermal conductivities of the wick and working fluid. Table 2 lists the configurations of the evaporator used in the simulations. The results of simulations 1, 2, and 3 are presented in this section. Those of simulations 4 and 5 are presented in the next section. Fluid properties are calculated using REFPROP [14], and temperature dependence is taken into account. The porous characteristics are the same in all the wicks. The bulk thermal conductivity of stainless steel (SS), PTFE, and copper are 16, 0.25, and 386 W/m-K, respectively. The contact angle is  $0^\circ$  under all conditions. The saturation temperature of the compensation chamber (CC) is  $29.4^\circ\text{C}$ . The groove saturation temperature is calculated from the pressure loss through the vapor line, condenser, and liquid line.

The heat flux applied to the evaporator is varied from  $0.3125\text{ W/cm}^2$  to the maximum heat flux of vapor penetration into the CC. The transition heat fluxes to the unsaturated wick, which satisfy Eq. (2), are listed in Table 3. The transition heat flux of the PTFE wick is the lowest. The simulation could not run at less than  $0.3125\text{ W/cm}^2$ . The reason for the low transition heat flux of the PTFE wick is that the temperature distribution at the contact surface between the wick and case is large owing to its low thermal conductivity. The transition heat fluxes using water as the working fluid vary from 1.7 to  $100\text{ W/cm}^2$ , as seen in the previous studies listed in Table 1. Results of this simulation is in this range as shown in Table 3. The relationship of the transition heat flux with the

wick thermal conductivity and pore radius cannot be found. The presence of non-condensation gas, surface roughness of the evaporator case, and condition of contact between the case and wick may affect the transition heat flux critically. The prediction of the transition heat flux seems to be complicated. Therefore, in the future, measurements should be performed to investigate vapor nucleation in a porous medium.

The boiling incipient superheat,  $\Delta T_{nuc}$  in Eq. (2), is calculated for the working fluid used in LHPs. The temperature dependence of fluid properties is taken into account. The nucleus radius is  $1.2\ \mu\text{m}$ . The results are presented in Fig. 5. Water shows the highest  $\Delta T_{nuc}$  value among all the fluids considered. Fluids that are at high pressure at room temperature, such as ammonia, have low boiling incipient superheat values; therefore, they are subject to transitions to the unsaturated state at low heat flux.

Fig. 6 presents the evaporator heat-transfer coefficient for each evaporator configuration. The evaporator heat-transfer coefficient is calculated as

$$h_{evap} = \dot{q}_{apply} / (T_{e,max} - T_{sat}) \quad (4)$$

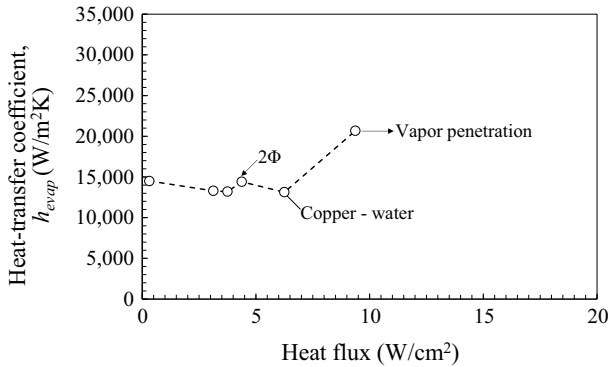
where  $T_{e,max}$  is the maximum temperature of the case and  $T_{sat}$  is the groove saturation temperature. In the copper-water LHP, vapor penetration occurs at  $12.5\text{ W/cm}^2$ . The pressure loss through the vapor line, condenser, and liquid line is  $76\text{ kPa}$  against a capillary pressure of  $100\text{ kPa}$  at the maximum heat flux. Hence, the pressure loss of the transport line is dominant. Because water has a high transition heat flux, the heat flux at the capillary limit can be comparable to the transition heat flux for the unsaturated state. Therefore, during the design of the optimum evaporator shape of the copper-water LHP, it is reasonable to assume that the phase state is saturated with liquid.

The evaporator heat-transfer coefficient of the ammonia LHP reaches a local maximum in the unsaturated state and decreases with an increase in the heat flux. Such heat-transfer characteristics have been measured in some LHP experiments [15–17]. These characteristics can be explained as follows. When the wick is unsaturated, due to increasing liquid-vapor interface area, the heat-transfer coefficient increases with increasing the heat. While, due to an increasing vapor phase in the wick, the heat-transfer coefficient also decreases with increasing the heat. This is because the liquid-vapor interface is far from the heating surface. Due to above two reasons, the heat-transfer coefficient for the unsaturated wick has a local maximum characteristic as shown in Fig. 6 (b). The local maximum characteristics of the evaporator heat-transfer coefficient is discussed in detail in Refs. [8,21]. Because the transition heat flux is much lower than the heat flux at the capillary limit, it is reasonable to assume that the phase state is that of an unsaturated wick with vapor and liquid when designing the optimum evaporator shape of an ammonia LHP.

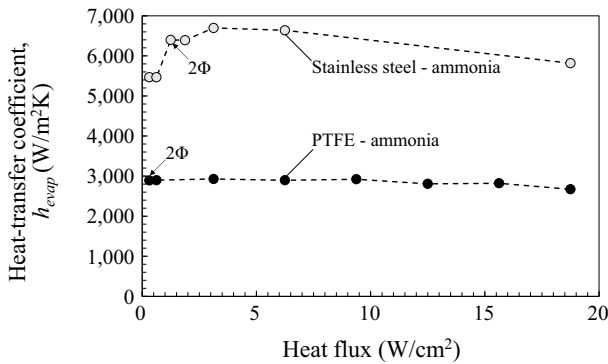
The heat-transfer coefficient of the copper-water LHP is several times higher than those of the other two LHPs. Jump characteristics are found in Fig. 6(a). Because the evaporator heat-transfer coefficient is dominated by thermal conduction from the heating surface to liquid-vapor interface in or on the wick, a higher thermal conductive wick benefits more from the effect of the interface area increasing. On comparison between the copper-water and SS-ammonia LHPs, bulk thermal conductivity of copper and SS are  $16\text{ W/m-K}$  and  $400\text{ W/m-K}$ , therefore the difference is 25 times. It is considered that such a large difference directly affects the jump of the evaporator heat-transfer coefficient from a saturated to an unsaturated state.

To analyze the heat flow structure in the evaporator, the heat flux vector is calculated as

$$\dot{q}^* \equiv \frac{-k_{eff} \nabla T}{-q_{apply}} \quad (5)$$



(a) Copper-water LHP



(b) Stainless steel-ammonia and PTFE-ammonia LHPs

Fig. 9. Evaporator heat-transfer coefficient as function of heat flux. Circumferential and axial grooves are created. The TPCL length is  $640\text{ m}^{-1}$ .

where  $k_{eff}$  is the effective thermal conductivity of the wick. The analysis results are presented in Fig. 7. Fig. 7 also presents the liquid-vapor interface. In terms of phase distribution, the SS-ammonia and PTFE-ammonia LHPs show the vapor phase at the center of the wick. On the other hand, the vapor phase for the copper-water LHP appears on a section of the three-phase contact line (TPCL) within the case, wick, and grooves and does not exist at the center of the wick. This is because  $\Delta T_{nuc}$  of water is much higher. The difference of the phase distribution leads to the particular characteristics of the heat-transfer coefficient for the copper-water evaporator.

The heat applied from the top of the case concentrates at the TPCL within the case, wick, and grooves as the high flux is shown in red arrows, and then transfers to the grooves by evaporation. The difference in the distribution of the heat flow depends on the

thermal conductivity of the wick and maximum heat fluxes at the TPCL, which are 5.68, 17.5, and 2.88 in the SS-ammonia, PTFE-ammonia, and copper-water LHPs, respectively. The heat flux at the bottom of the PTFE wick is low, so the heat leak to the CC is the lowest for this case. In this paper, the discussion is focused on only the evaporator, but when the performance of an LHP system is considered, the amount of the heat leak should be included in the discussion.

Because the heat flux concentrates at the TPCL in any phase state, it is considered that the evaporator heat-transfer coefficient can be enhanced by making the TPCL longer. This simulation is presented in the next section. A TPCL length of  $500 \text{ m}^{-1}$  is considered in the present section. Note that the TPCL length is represented as the area density of the heat-load area; therefore, the unit is  $\text{m}^{-1}$ .

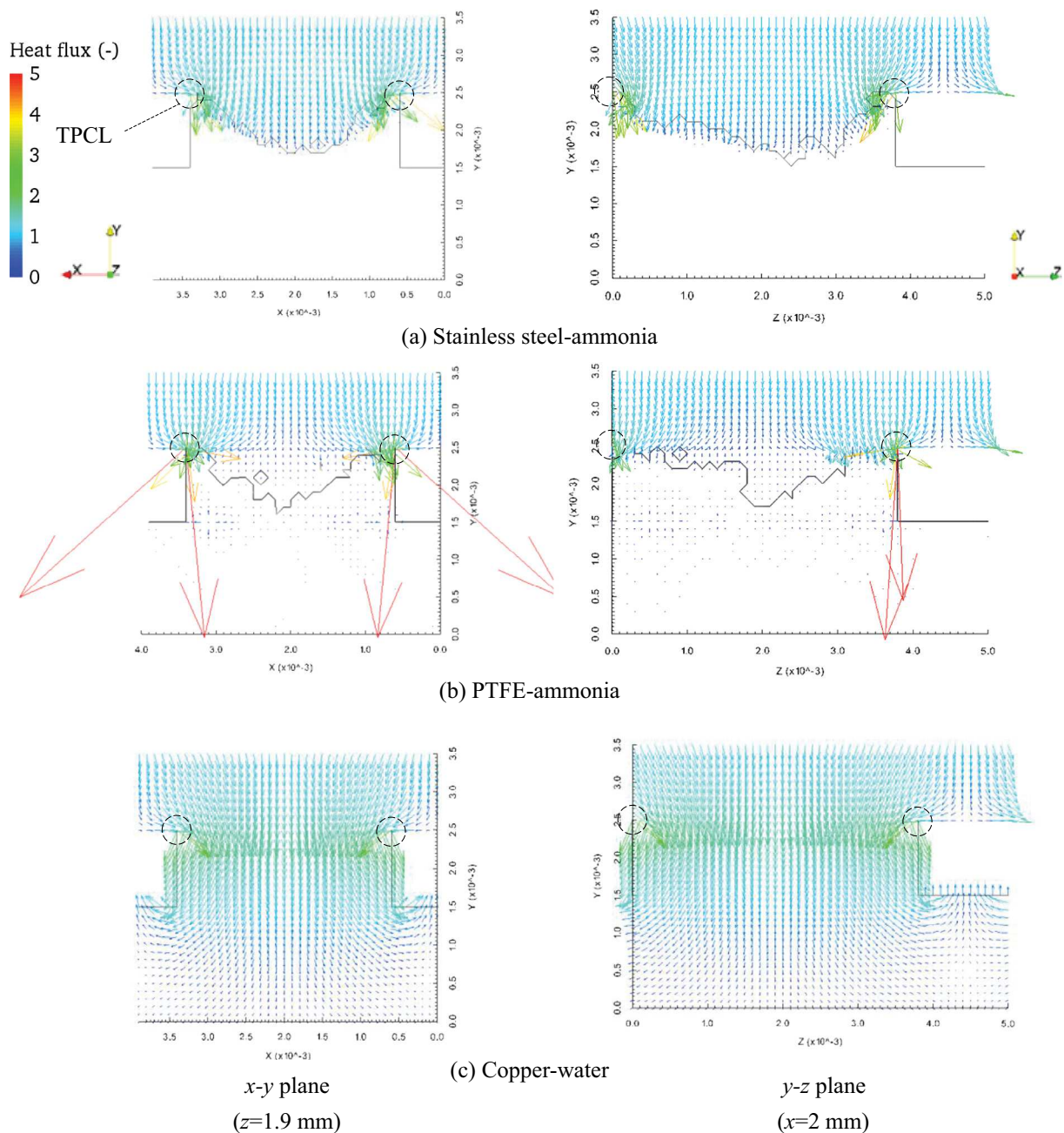


**Fig. 10.** Distribution of heat flux vectors and liquid-vapor interface shape on  $x$ - $y$  and  $y$ - $z$  plane. The color bar is normalized with an applied heat flux. The applied heat flux is  $6.25 \text{ W/cm}^2$ . Both axial and circumferential grooves are created. The TPCL length is  $640 \text{ m}^{-1}$ .

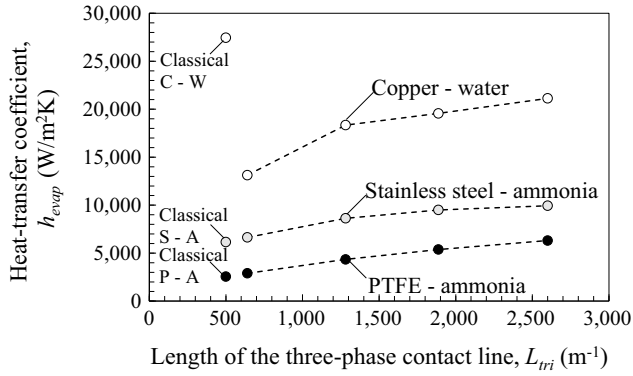


**Fig. 11.** Evaporator heat-transfer coefficients of copper-water, SS-ammonia, and PTFE-ammonia LHPs as function of TPCL length. The applied heat flux is  $6.25 \text{ W/cm}^2$ . The number of circumferential and axial grooves increases with an increase in the TPCL length.

## 4. Three-dimensional groove shape

### 4.1. Calculation domain and boundary conditions

The computational domain is depicted in Fig. 8. Circumferential grooves as well as axial grooves are created to make the TPCL longer. The circumferential groove approach has been proposed in Refs. [18,19], and the improvement of the evaporator heat-transfer coefficient has been verified experimentally. To compare the axial groove configurations only, the area of the contact surface between the case and wick is maintained to be the same (0.5) in the ratio of this area to the area of the heat load. In the case of a cylindrical evaporator, the axial length is longer, so the TPCL can be made longer by increasing the number of circumferential grooves. In this simulation, the width of the axial groove is equal to that of the circumferential groove. For this shape, the contact surface is square and the TPCL length is  $640 \text{ m}^{-1}$ .

The boundary conditions are explained as follows. A spatial periodic boundary is imposed at  $z=0, L_z$ , except on the upper side of the wick. At the wick-groove interface with  $z=0, L_z-L_z_g$ , when the wick phase is saturated, the boundary conditions are given by

$$-k_{eff} \frac{\partial T}{\partial n} \Big|_{\Gamma} = h_i(T - T_{gr}) \quad \text{and} \quad (6)$$

$$\dot{m}_n = \frac{h_i A (T - T_{gr})}{H_{fg}} \quad (7)$$

and when the wick phase is unsaturated, they are given by

$$-k_{eff} \frac{\partial T}{\partial n} \Big|_{\Gamma} = h_c(T - T_{gr}) \quad \text{and} \quad (8)$$

$$P = P_{gr} \quad (9)$$

where  $h_i$  is the interfacial heat-transfer coefficient [20]. These boundary conditions are the same as the conditions at the wick-groove interface in the  $x$  direction. The other boundary conditions are the same as those described in the previous section.

## 4.2. Results and discussion

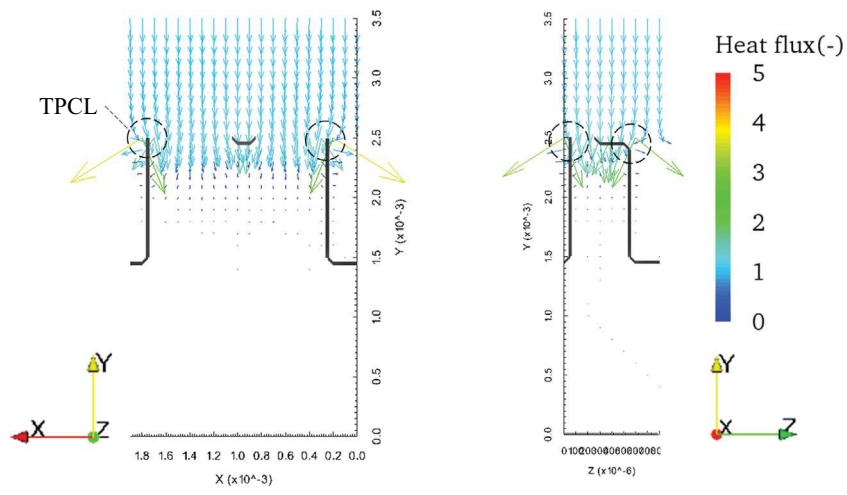
Fig. 9 presents the results of the evaporator heat-transfer coefficient as a function of the heat flux. Fig. 10 presents the distribution of the heat flux vectors defined in Eq. (5) on the  $x$ - $y$  and  $y$ - $z$  planes. The maximum heat-transfer coefficient for the SS-ammonia LHP is  $6600 \text{ W/m}^2\cdot\text{K}$ , which is higher than that for the LHP with only axial grooves ( $6100 \text{ W/m}^2\cdot\text{K}$ ). The maximum heat flux at the TPCL for the SS-ammonia LHP is 3.96, which is smaller than that for the LHP with only axial grooves. The evaporator heat-transfer coefficient for the copper-water LHP does not increase. The maximum heat flux is 2.63, which is smaller than that for the LHP with only axial grooves. The reason why the evaporator heat-transfer coefficient of the copper-water LHP did not increase may be related to the increasing of the liquid-vapor interface area on the unsaturated wick against the saturated wick. When the TPCL length is  $640/\text{m}$  (Fig. 10), the increasing of the liquid-vapor interface area on the unsaturated wick is 1.0004, which is the ratio to the interface area of the saturated wick. While, the increasing liquid-vapor interface area with  $500/\text{m}$  (Fig. 7) is 1.1. Benefit of the increasing liquid-vapor interface area may be more dominant than the benefit of the increasing of the TPCL length.

Fig. 11 presents the evaporator heat-transfer coefficient of each configuration as a function of the TPCL length. The length is divided by the area of the heat load. The TPCL length changes with the width and number of both the axial and circumferential grooves. The area of the contact surface between the case and wick is constant (0.5). All the phase states of the wick shown in Fig. 11 are unsaturated. The results for the classical wick shape with  $500 \text{ m}^{-1}$  TPCL length were also presented in Fig. 11. The heat-transfer coefficient increases with an increase in the TPCL length in any configuration except the classical copper-water LHP. The maximum heat-transfer coefficient for the SS-ammonia LHP is  $9900 \text{ W/m}^2\cdot\text{K}$  when the TPCL length is  $2600 \text{ m}^{-1}$ , and both the groove widths are 0.3 mm. It is found that the evaporator heat-transfer coefficient can be enhanced by making the TPCL longer. However, when the TPCL is very long, because the groove width is very small, the effect of the distribution of saturation pressure in the grooves cannot be neglected. Therefore, it is considered that the optimum shape of the LHP evaporator can be designed by establishing a trade-off between an increase in the heat-transfer coefficient achieved by increasing the TPCL length and the effect of increasing pressure loss in the grooves. The proposed method for optimization of wick shape is presented in Ref. [22]. In addition, a detailed heat-transfer simulation at the TPCL should be performed in the future.

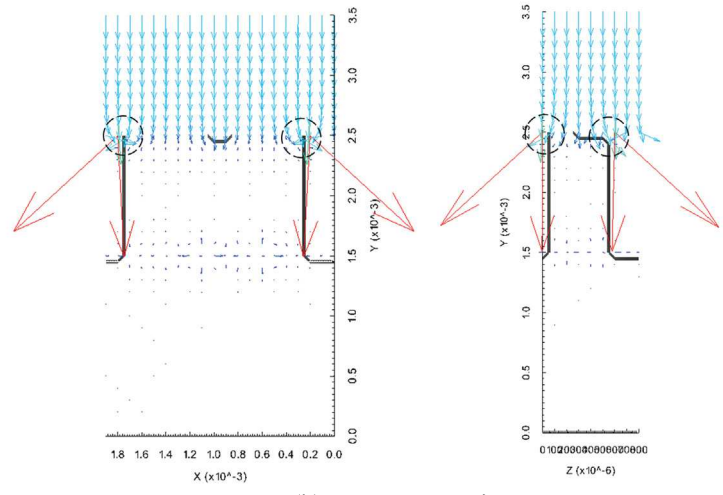
Fig. 12 presents the distribution of the heat flux vectors on the  $x$ - $y$  and  $y$ - $z$  planes when the TPCL length is  $2600 \text{ m}^{-1}$ . For SS-ammonia and PTFE ammonia LHPs, the maximum heat flux decreases and homogenization is promoted. However, for copper-water LHP, the maximum heat flux is high due to vapor phase is formed at the TPCL. Because the copper-water LHP has peculiar characteristics of vapor pocket, further studies for the heat transfer mechanism and the method for optimization of wick shape is needed.

Fig. 13 presents the evaporator heat-transfer coefficients of two SS-ammonia LHPs as a function of the TPCL length. One LHP has only axial grooves, whereas the other has both axial and circumferential grooves. There is little difference in the effects of the TPCL length between the two LHP types. The width of the grooves in the configuration with only axial grooves is smaller than that in the configuration with both groove types for the same TPCL length. Therefore, the configuration with only axial grooves can experience problems during wick manufacturing.

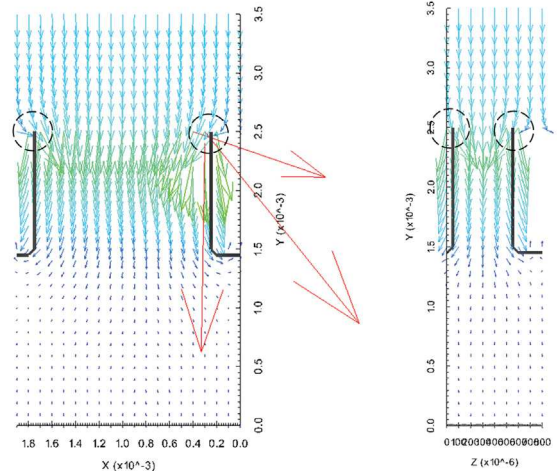




(a) Stainless steel-ammonia



(b) PTFE-ammonia



(c) Copper-water

x-y plane

y-z plane

Fig. 12. Distribution of heat flux vectors and liquid-vapor interface shape on x-y and y-z plane. The applied heat flux is 6.25 W/cm<sup>2</sup>. Both axial and circumferential grooves are created. The TPCL length is 2600 m<sup>-1</sup>.

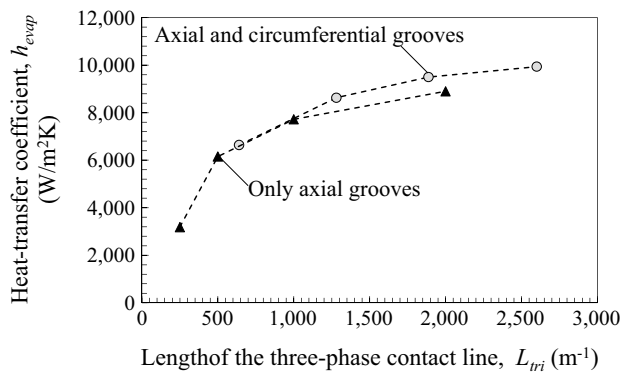


**Fig. 13.** Evaporator heat-transfer coefficient of SS-ammonia LHP as function of TPCL length. The applied heat flux is  $6.25 \text{ W/cm}^2$ .

## 5. Conclusions

This paper presented heat-transfer simulations in LHP evaporators using a three-dimensional pore network model. The results for different combinations of the wick material and working fluid, namely, SS-ammonia, PTFE-ammonia, and copper-water, were calculated for an evaporator with only axial grooves and for one with both circumferential and axial grooves.

- I. The effect of the thermal conductivity of the wick and working fluid on the transition heat flux from a saturated wick with liquid to an unsaturated wick with vapor and liquid was presented. Because different transition heat fluxes were obtained, when the optimum evaporator shape of the ammonia LHP was designed, it was reasonable to assume the phase state to be that of an unsaturated wick for the ammonia LHPs and that of a saturated wick for the copper-water LHPs.
- II. It was found that heat flux concentrated at the TPCL within the case, wick, and grooves. The evaporator heat-transfer coefficients of the SS-ammonia, PTFE-ammonia, and copper-water LHPs were increased with increasing the TPCL length except the classical wick shape of the copper-water LHP. Results indicated that the optimum shape of the evaporator could be realized by adjusting the TPCL length.

In the future, detailed heat-transfer simulation at the TPCL should be performed.

## Acknowledgement

This research was partly supported by JSPS KAKENHI Grant Number 15H06287 and by JST, PRESTO. A super computer system in the Information Technology Center of Nagoya University was used for the calculations.

## References

- [1] C. Figus, Y. Le Bray, S. Bories, M. Prat, Heat and mass transfer with phase change in a porous structure partially heated: continuum model and pore

- network simulations, *Int. J. Heat Mass Transf.* 42 (1999) 2557–2569, [http://dx.doi.org/10.1016/S0017-9310\(98\)00342-1](http://dx.doi.org/10.1016/S0017-9310(98)00342-1).
- [2] T.S. Zhao, Q. Liao, On capillary-driven flow and phase-change heat transfer in a porous structure heated by a finned surface: measurements and modeling, *Int. J. Heat Mass Transf.* 43 (2000) 1141–1155, [http://dx.doi.org/10.1016/S0017-9310\(99\)00206-9](http://dx.doi.org/10.1016/S0017-9310(99)00206-9).
- [3] T. Kaya, J. Goldak, Numerical analysis of heat and mass transfer in the capillary structure of a loop heat pipe, *Int. J. Heat Mass Transf.* 49 (2006) 3211–3220, <http://dx.doi.org/10.1016/j.ijheatmasstransfer.2006.01.028>.
- [4] Z.M. Wan, W. Liu, Z.K. Tu, A. Nakayama, Conjugate numerical analysis of flow and heat transfer with phase change in a miniature flat plate CPL evaporator, *Int. J. Heat Mass Transf.* 52 (2009) 422–430, <http://dx.doi.org/10.1016/j.ijheatmasstransfer.2008.06.019>.
- [5] M.A. Chernysheva, Y.F. Maydanik, 3D-model for heat and mass transfer simulation in flat evaporator of copper-water loop heat pipe, *Appl. Therm. Eng.* 33 (2012) 124–134, <http://dx.doi.org/10.1016/j.applthermaleng.2011.09.025>.
- [6] M.A. Chernysheva, Y.F. Maydanik, Simulation of thermal processes in a flat evaporator of a copper-water loop heat pipe under uniform and concentrated heating, *Int. J. Heat Mass Transf.* 55 (2012) 7385–7397, <http://dx.doi.org/10.1016/j.ijheatmasstransfer.2012.07.001>.
- [7] L. Ji, G.P. Peterson, 3D heat transfer analysis in a loop heat pipe evaporator with a fully saturated wick, *Int. J. Heat Mass Transf.* 54 (2011) 564–574, <http://dx.doi.org/10.1016/j.ijheatmasstransfer.2010.09.014>.
- [8] L. Mottet, T. Coquard, M. Prat, Three dimensional liquid and vapour distribution in the wick of capillary evaporators, *Int. J. Heat Mass Transf.* 83 (2015) 636–651, <http://dx.doi.org/10.1016/j.ijheatmasstransfer.2014.12.048>.
- [9] M. Nishikawara, H. Nagano, L. Mottet, M. Prat, Formation of unsaturated regions in the porous wick of a capillary evaporator, *Int. J. Heat Mass Transf.* 89 (2015) 588–595, <http://dx.doi.org/10.1016/j.ijheatmasstransfer.2015.05.054>.
- [10] M. Nishikawara, H. Nagano, M. Prat, Evaporator heat-transfer analysis of a loop heat pipe with low thermal conductivity wicks, in: *Proceedings of the 17th International Heat Pipe Conference*, No. 18, Kanpur, October 2013.
- [11] M. Nishikawara, H. Nagano, L. Mottet, M. Prat, Numerical study of thermal performance of a capillary evaporator in a loop heat pipe with liquid-saturated wick, *J. Electron. Cool. Therm. Contr.* 27 (2014) 118–127, <http://dx.doi.org/10.4236/jectc.2014.44013>.
- [12] M. Nishikawara, H. Nagano, Numerical simulation of capillary evaporator with microgap in a loop heat pipe, *Int. J. Therm. Sci.* 102 (2016) 39–46, <http://dx.doi.org/10.1016/j.ijthermalsci.2015.11.008>.
- [13] R. Hatakenaka, A. Okamoto, Y. Mase, M. Murakami, H. Iikura, Visualization of internal fluid behavior in a miniature loop heat pipe using neutron radiography, in: *41st International Conference on Environmental Systems, International Conference on Environmental Systems (ICES), AIAA 2011-5140*, Oregon, July 2011, <http://dx.doi.org/10.2514/6.2011-5140>.
- [14] E.W. Lemmon, M.L. Huber, M.O. McLinden, NIST Standard Reference Database 23: Reference Fluid Thermodynamic and Transport Properties-REFPROP, Version 9.1, National Institute of Standards and Technology, Standard Reference Data Program, Gaithersburg, 2013.
- [15] M. Nishikawara, H. Nagano, Parametric experiments on a miniature loop heat pipe with PTFE wicks, *Int. J. Therm. Sci.* 85 (2014) 29–39, <http://dx.doi.org/10.1016/j.ijthermalsci.2014.05.016>.
- [16] S.V. Vershinin, Y.F. Maydanik, Hysteresis phenomena in loop heat pipes, *Appl. Therm. Eng.* 27 (2007) 962–968, <http://dx.doi.org/10.1016/j.applthermaleng.2006.08.016>.
- [17] R. Singh, A. Akbarzadeh, M. Mochizuki, Effect of wick characteristics on the thermal performance of the miniature loop heat pipe, *J. Heat Transf.* 131 (2009) 082601, <http://dx.doi.org/10.1115/1.3109994>.
- [18] R.R. Riehl, N. dos Santos, Loop heat pipe performance enhancement using primary wick with circumferential grooves, *Appl. Therm. Eng.* 28 (2008) 1745–1755, <http://dx.doi.org/10.1016/j.applthermaleng.2007.11.005>.
- [19] M. Kuroi, H. Nagano, The influence of groove shape on loop heat pipe performance, *Heat Pipe Sci. Technol. Int. J.* 3 (2012) 203–222, <http://dx.doi.org/10.1615/HeatPipeSciTech.2013006554>.
- [20] V.P. Carey, *Liquid-Vapor Phase-Change Phenomena*, second ed., Taylor & Francis, 2008, pp. 107–112.
- [21] M. Nishikawara, H. Nagano, Numerical analysis of liquid-vapor thermo-fluid behavior in a loop heat pipe evaporator with pore network model (liquid-vapor phase distribution in a porous structure and heat-transfer characteristics), *Therm. Sci. Eng.* 23 (4) (2015) 71–80, <http://dx.doi.org/10.11368/tse.23.71> (in Japanese).
- [22] M. Nishikawara, H. Nagano, Optimization of wick shape in a loop heat pipe for high heat transfer, *Int. J. Heat Mass Transf.* 104 (2017) 1083–1089, <http://dx.doi.org/10.1016/j.ijheatmasstransfer.2016.09.027>.